22

Relativistic Nonlinear Thomson Scattering: Toward Intense Attosecond Pulse

Kitae Lee[1], Sang-Young Chung[2], and Dong-Eon Kim[3]
[1]*Korea Atomic Energy Research Institute,*
[2]*Pusan national University,*
[3]*Pohang University of Science and Technology*
Republic of Korea

1. Introduction

Over many millennia of human history, mankind has been interested in how events change in time, namely their dynamics. However, the time resolution of recording individual steps has been limited to direct sensory perception such as the eye's ability (0.1 sec. or so) to recognize the motion, until 1800 AD when the technical revolution occurred following the industrial revolution. A famous motion picture of a galloping horse by E. Muybridge in 1878 is a good example of the technological development in time-resolved measurement. By this time, the nanosecond time resolution has been achieved; however, it took another century to break the nanosecond barrier as shown in Fig.1. The Advent of a laser has paved ways to ever shorter time resolution: in the 1980's, the picosecond barrier was broken and the femtosecond science and technology has rapidly progressed in the 1990's; at the turn of the 21st century, the femtosecond barrier has been broken (Hantschel et al., 2001), opening up the era of attosecond science and technology. The current shortest duration of a pulse achieved is 80 attoseconds around 100 eV of photon energy (Goulielmakis et al., 2008).

Femtosecond science and technology have allowed us to explore various ultrafast phenomena in physical (Siders et al., 1999), chemical (Zewail, 2000) and biological (Vos et al., 1999) systems. A great number of ultrafast atomic motions in biology, chemistry, and physics have been investigated with optical probes. In physics, the nature of atomic re-arrangements during phase transitions and the relation between amorphous, liquid and crystalline states has been interest (Afonso et al., 1996; Huang et al., 1998). Along with much interest in spintronics during the last decade, efforts have been made to understand spin dynamics in various pure and complex magnetic systems. In chemistry, the real time observation of atomic motions in chemical reactions has been long thought for. Femtosecond optical and IR technology has served this purpose in excellent ways. Femtosecond pulses have pumped molecules to create wavepackets. The observation of the motion of the wavepackets using femtosecond pulse probe or other methods has provided rich information on chemical reactions (Zewail, 2000). The various chemical bonds such as covalent, ionic, dative, metallic, hydrogen and van der Waals bonds have been studied in the varying complexity of molecular systems from diatomics to proteins and DNA. All of

Source: Advances in Solid-State Lasers: Development and Applications, Book edited by: Mikhail Grishin,
ISBN 978-953-7619-80-0, pp. 630, February 2010, INTECH, Croatia, downloaded from SCIYO.COM

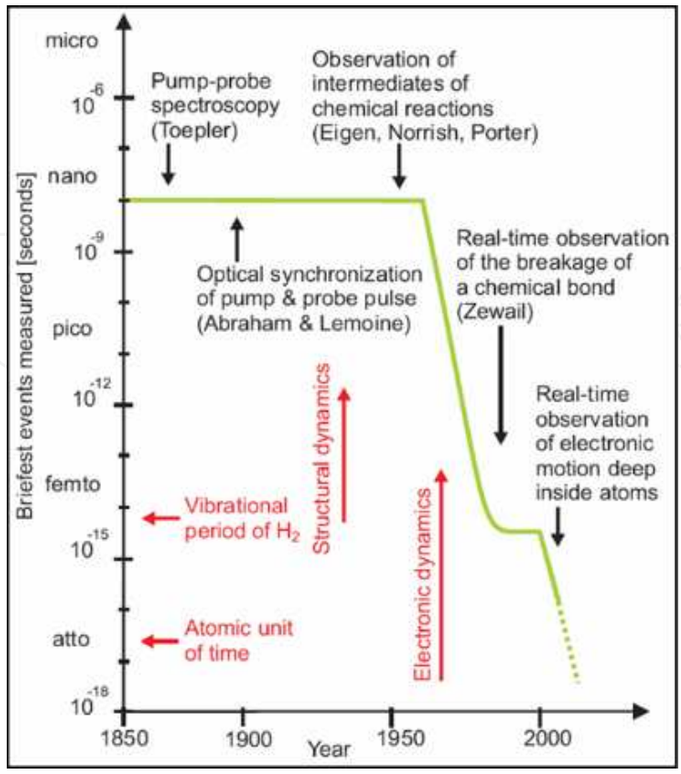

Fig. 1. Evolution of techniques for real-time observation of microscopic processes (Krausz et al., 2009).

these successful applications of femtosecond optical technology to follow reaction dynamics in chemistry have led to the award of Nobel prize to Prof. Zewail in 1999 who has initiated femtochemistry in the 1990's. There are also many fundamental biological processes taking place in femtosecond time scale. Good examples are photo-induced isomerizations (Gai et al., 1998) and ligand dissociations (Perutz et al., 1998). Femtosecond optical pulses have been used for the investigation of these processes.

During the last several years, isolated attosecond pulses have been successfully exploited to control the localization of electron under chemical reaction (Kling et al., 2006), observe inner shell transitions in atoms (Drescher et al., 2002), and electron tunneling across Coulomb barrier (Uiberacker et al., 2007), electron transport in condensed matter (Cavalieri et al., 2007).

The demand on and the emphasis to the understanding of the ultrafast phenomena and the control of them is ever increasing. The Department of Energy of the United States of America asked the Basic Energy Science Advisory Committee (BESAC) to identify grand challenges in science to be pursued in the 21st century. The BESAC has identified 5 grand challenges in their report, the summary of which has been published in the July issue of Physics Today in 2008 (Fleming & Ratner, 2008). The first of the grand challenges is to control material properties at the level of electronic motion. The report recommended the development of attosecond and femtosecond metrology to measure and control electron dynamics.

Optical or ultraviolet light allows one to probe the dynamical changes of excited electronic states in a sample. This is the core of interest in many research topics such as electron-hole dynamics in solids, or excitation transfer in photosynthesis, bond breaking in chemical

reactions. However, no or partial information on structure can be obtained if the process under investigation involves the structural changes.

X-ray imaging or diffraction has the potential to provide a global picture of structural changes in the fields of atomic and molecular physics, plasma physics, material science, chemistry and life science (Bloembergen, 1999; http://tesla.desy.de/new_pages /TDR_CD/PartV/fel.html). Since x-ray photons are scattered from all the electrons in a sample, the intensity of diffraction is directly related to the electronic density. Since the structural changes occur in the time scale of 100 fs or so, following the charge re-arrangement, the electronic density measured in this time scale closely reflects the atomic structure. On the other hand, attosecond x-ray pulse will enable us to follow even faster motions of electrons in intra-atomic or intra-molecular processes, which has not been achieved yet because of the lack of such sources.

Femtosecond time-resolved x-ray diffraction experiments have been used to study structural processes such as the observation of atomic structure and dynamics [18], the investigation of ultrafast phase transition in solid (Gaffney & Chapman, 2008) and time-resolved biomolecular imaging (Sokolowski-Tinten et al., 2003). These results are very impressive and of landmark: however, there are still many phenomena yet to be explored and a variety of attosecond and femtosecond X-ray sources yet to be further developed. They comprise a great challenge to the scientific community.

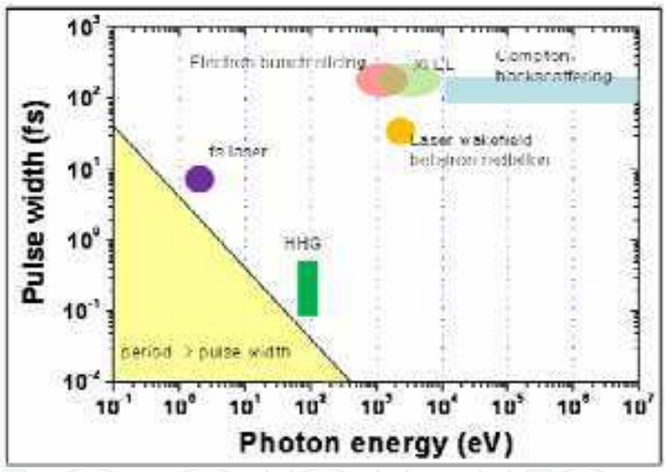

Fig. 2. Currently-available ultrafast light sources are plotted in terms of photon energy and pulse duration.

Figure 2 shows ultrafast sources available currently or in the immediate future. It is conspicuous that there is no source available in keV or higher energies faster than 10 fs. In fact, for wider exploration and manipulation of electron dynamics in a vast spectrum of natural phenomena, attosecond or a few fs keV pulses are demanded.

Several schemes have been proposed and/or demonstrated to generate an ultrashort keV x-ray pulse: the relativistic Doppler shift of a backscattered laser pulse by a relativistic electron beam (Sprangle et al., 1992; Hartemann, 1998; Esarey et al., 1993a; Chung et al., 2009), the harmonic frequency upshift of a laser pulse by relativistic nonlinear motion of electrons (Vachaspati, 1962; Brown & Kibble, 1964; Esarey et al,, 1992; Chen et al., 1998, 2000; Ueshima et al, 1999; Kaplan & Shkolnikov, 2002; Banerjee et al., 2002; Lee et al., 2003a, 2003b, 2005, 2008; Phuoc et al., 2003; Kim et al., 2009), high order harmonic generation in the interaction

of intense laser pulse with solids (Linde et al., 1995, 1996, 1999; Norreys et al., 1996; Lichters et al., 1996; Tarasevitch et al., 2000) and x-ray laser using inner shell atomic transitions (Kim et al., 1999, 2001).

Ultrafast high-intensity X-rays can be generated from the interaction of high intensity femtosecond laser via Compton backscattering (Hartemann et al., 2005), relativistic nonlinear Thomson scattering (Ueshima et al., 1999; Kaplan & Shkolnikov 2002; Banerjee et al., 2002) and laser-produced betatron radiation (Phuoc et al., 2007). In synchrotron facilities, electron bunch slicing method has been adopted for experiments (Schoenlein, 2000; Beaud et al., 2007). Moreover, X-ray free electron lasers (Normile, 2006) were proposed and have been under construction. The pulse duration of these radiation sources are in the order of a few tens to hundred fs. There are growing demands for new shorter pulses than 10 fs.

The generation of intense attosecond or femtosecond keV lights via Thomson scattering (Lee et al., 2008; Kim et al., 2009) is attractive, because the radiation is intense and quasi-monochromatic. This radiation may be also utilized in medical (Girolami et al., 1996) and nuclear physics (Weller & Ahmed, 2003) area of science and technology.

When a low-intensity laser pulse is irradiated on an electron, the electron undergoes a harmonic oscillatory motion and generates a dipole radiation with the same frequency as the incident laser pulse, which is called Thomson scattering. As the laser intensity increases, the oscillatory motion of the electron becomes relativistically nonlinear, which leads to the generation of harmonic radiations. This is referred to as **relativistic nonlinear Thomson scattered (RNTS) radiation**. The RNTS radiation has been investigated in analytical ways (Esarey et al., 1993a; Chung et al., 2009; Vachaspati, 1962; Brown et al., 1964; Esarey & Sprangle, 1992; Chen et al., 1998; Ueshima et al., 1999; Chen et al., 2000; Kaplan & Shkolnikov, 2002; Banerjee et al., 2002). Recently, such a prediction has been experimentally verified by observing the angular patterns of the harmonics for a relatively low laser intensity of 4.4×10^{18} W/cm^2 (Lee et al., 2003a, 2003b). Esarey *et al.* (Esarey et al., 1993a) has investigated the plasma effect on RNTS and presented a set of the parameters for generating a 9.4-ps x-ray pulse with a high peak flux of 6.5×10^{21} photons/s at 310 eV photon energy using a laser intensity of 10^{20} W/cm^2. Ueshima *et al.* (Ueshima et al., 1999) has suggested several methods to enhance the radiation power, using particle-incell simulations for even a higher intensity. Kaplan and Shkolnikov *et al.* (Kaplan & Shkolnikov, 2002) proposed a scheme for the generation of zeptosecond (10^{-21} sec) radiation using two counter-propagating circularly polarized lasers, named as lasertron.

Recently, indebted to the development of the intense laser pulse, experiments on RNTS radiation have been carried out by irradiating a laser pulse of 10^{18}–10^{20} W/cm^2 on gas jet targets (Kien et al., 1999; Paul et al., 2001; Hertz et al., 2001). A numerical study in the case of single electron has been attempted to characterize the RNTS radiation (Kawano et al., 1998) and a subsequent study has shown that it has a potential to generate a few attosecond x-ray pulse (Harris & Sokolov, 1998). Even a scheme for the generation of a zeptosecond x-ray pulse using two counter propagating circularly polarized laser pulses has been proposed (Kaplan & Shkolnikov, 1996).

In this chapter, we concern RNTS in terms of the generation of ultrafast X-ray pulses. The topics such as fundamental characteristics of RNTS radiations, coherent RNTS radiations, effects of the high-order fields (HOFs) under a tight-focusing condition, and generation of an intense attosecond x-ray pulse will be discussed in the following sections.

2. Fundamental characteristics of RNTS radiations

In this section, the dynamics of an electron under an ultra-intense laser pulse and some fundamental characteristics of the RNTS radiations will be discussed (Lee et al., 2003a, 2003b).

2.1 Electron dynamics under a laser pulse

The dynamics of an electron irradiated by a laser field is obtained from the relativistic Lorentz force equation:

$$\frac{d}{dt}\left(\gamma\vec{\beta}\right) = -\frac{e}{m_e c}\left(\vec{E}_L + \vec{\beta}\times\vec{B}_L\right), \tag{1}$$

The symbols used are: electron charge (e), electron mass (m_e), speed of light (c), electric field ($\vec{E}_L$), magnetic field ($\vec{B}_L$), velocity of the electron divided by the speed of light ($\vec{\beta}$), and relativistic gamma factor ($\gamma = 1/\sqrt{1-\beta^2}$). It is more convenient to express the laser fields with the normalized vector potential, $\vec{a} = e\vec{E}_L / m_e\omega_L c$, where ω_L is the angular frequency of the laser pulse. It can be expressed with the laser intensity I_L in W/cm² and the laser wavelength λ_L in micrometer as below:

$$a = 8.5\times10^{-10}\lambda_L\sqrt{I_L}\ . \tag{2}$$

Eq. (1) can be analytically solved under a planewave approximation and a slowly-varying envelope approximation, which lead to the following solution (Esarey et al., 1993a):

$$\gamma\vec{\beta} = \gamma_o\vec{\beta}_o + \vec{a} + \frac{a^2 + 2\gamma_o\vec{a}\cdot\vec{\beta}_o}{2q_o}\hat{z}\,, \tag{3}$$

$$\gamma = \frac{\left|\vec{a} + \gamma_o\vec{\beta}_{o\perp}\right|^2 + 1 + q_o^2}{2q_o}\,, \tag{4}$$

where $q_o = \gamma_o\left(1-\beta_{oz}\right)$ and the subscript $\perp$ denotes the direction perpendicular to the direction of laser propagation (+z). The subscript, 'o' denotes initial values. When the laser

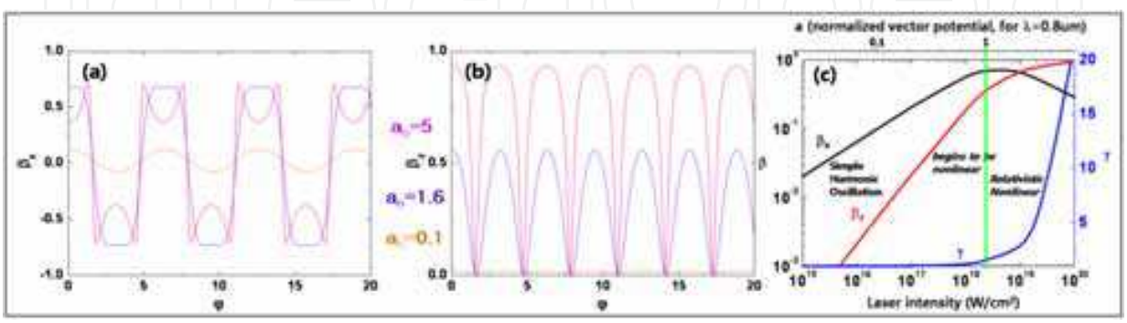

Fig. 3. Dynamics of an electron under a laser pulse: Evolution of (a) transverse and (b) longitudinal velocities, and (c) peak values on laser intensities. The initial velocity was set to zero for this calculation. Different colors correspond to different a_o's in (a) and (b).

intensity is low or $|a| << 1$, the electron conducts a simple harmonic oscillation but as the intensity becomes relativistic or $|a| \geq 1$, the electron motion becomes relativistically nonlinear. Figure 3 (a) and (b) show how the electron's oscillation becomes nonlinear due to relativistic motion as the laser intensity exceeds the relativistic intensity. One can also see that the drift velocity along the +z direction gets larger than the transverse velocity as $|a| \geq 1$ [Fig. 3 (c)].

2.2 Harmonic spectrum by a relativistic nonlinear oscillation

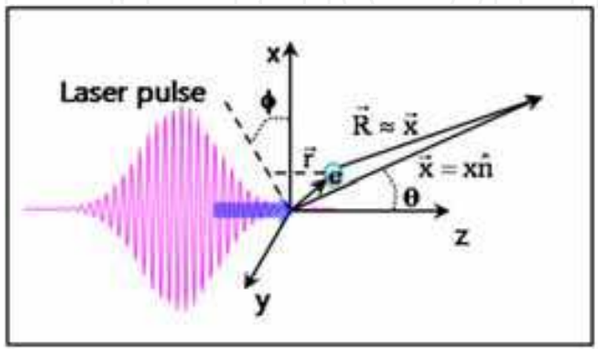

Fig. 4. Schematic diagram for the analysis of the RNTS radiations

Once the dynamics of an electron is obtained, the angular radiation power far away from the electron toward the direction, $\hat{n}$ [Fig. 4] can be obtained through the Lienard-Wiechert potential (Jackson, 1975)

$$\frac{dP(t)}{d\Omega} = \left|\vec{A}(t)\right|^2 \tag{5}$$

$$\vec{A}(t) = \sqrt{\frac{e^2}{4\pi c}}\left[\frac{\hat{n}\times\left\{\left(\hat{n}-\vec{\beta}\right)\times\dot{\vec{\beta}}\right\}}{\left(1-\hat{n}\cdot\vec{\beta}\right)^3}\right]_{t'} \tag{6}$$

where t' is the retarded time and is related to t by

$$t = t' + \frac{x - \hat{n}\cdot\vec{r}(t')}{c}. \tag{7}$$

Then the angular spectrum is obtained by

$$\frac{d^2I}{d\omega d\Omega} = 2\left|\vec{A}(\omega)\right|^2, \tag{8}$$

where $\vec{A}(\omega)$ is the Fourier transform of $\vec{A}(t)$. These formulae together with Eq. (1) are used to evaluate the scattered radiations. Under a planewave approximation, the RNTS spectrum can be analytically obtained (Esarey et al., 1993a). Instead of reviewing the analytical process, important characteristics will be discussed along with results obtained in numerical simulations.

Figure 5 shows how the spectrum is changed, as the laser intensity gets relativistic. The spectra were obtained by irradiating a linearly-polarized laser pulse on a counter-propagating relativistic electron with energy of 10 MeV, which is sometimes called as nonlinear Compton backscattering. One can see that higher order harmonics are generated as the laser intensity increase. It is also interesting that the spacing between harmonic lines gets narrower, which is caused by Doppler effect (See below). The cut-off harmonic number has been numerically estimated to be scaled on the laser intensity as $\sim a^3$ (Lee et al., 2003b).

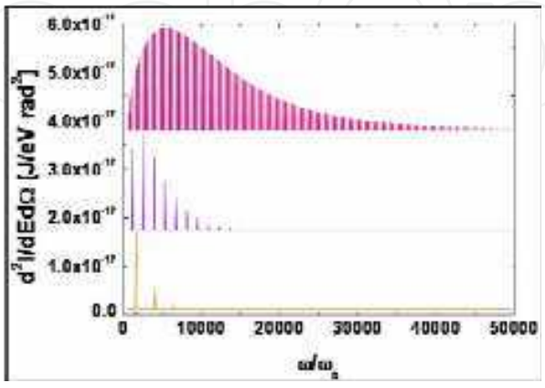

Fig. 5. Spectra of RNTS in a counter-propagating geometry for different laser intensities, a_o=0.1, 0.8, 1.6, and 5 from bottom. (The spectrum for a_o=0.1 is hardly seen due to its lower intensity.)

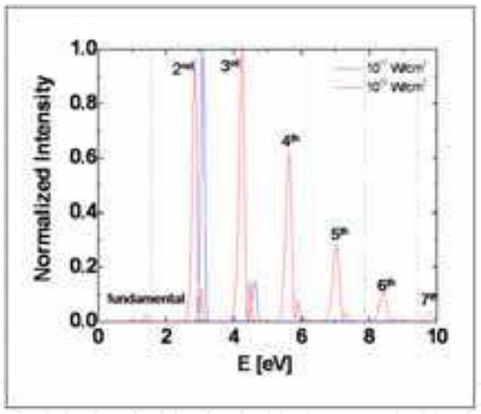

Fig. 6. Red-shift of harmonic frequencies on laser intensity. The spectra were obtained at the direction of $\theta = 90^o$ and $\phi = 0^o$ from an electron initially at rest. The vertical dotted lines indicate un-shifted harmonic lines. For this calculation, a linearly polarized laser pulse with a pulse width in full-with-half-maximum (FWHM) of 20 fs was used.

As shown in Fig. 6, the fundamental frequency, ω_1^s shifts to the red side as the laser intensity increases. This is caused by the relativistic drift velocity of the electron driven by $\vec{v} \times \vec{B}_L$ force. Considering Doppler shift, it can be obtained as (Lee et al., 2006)

$$\frac{\omega_1^s}{\omega_L} = \frac{4\gamma_o^2\left(1-\beta_{zo}\right)}{4\gamma_o^2\left(1-\vec{\beta}_o\cdot\hat{n}\right)+a_o^2\dfrac{\left(1-\cos\theta\right)}{\left(1-\beta_{zo}\right)}}. \tag{9}$$

In the case of an electron initially at rest ($\gamma_o = 1$, $\beta_o = 0$), this leads to the following formula

$$\frac{\omega_1^s}{\omega_L} = \frac{1}{1 + \frac{a_o^2}{4}\left(1 - \cos\theta\right)} . \tag{10}$$

Note that the amount of the red shift is different at different angles. The dependence on the laser intensity can be stated as follows. As the laser intensity increases, the electron's speed approaches the speed of light more closely, which makes the frequency of the laser more red-shifted in the electron's frame. No shift occurs in the direction of the laser propagation. The parasitic lines in the blue side of the harmonic lines are caused by the different amount of the red-shift due to rapid variation of laser intensity.

The angular distributions of the RNTS radiations show interesting patterns depending on harmonic orders [Fig. 7]. The distribution in the forward direction is rather simple, a dipole radiation pattern for the fundamental line and a two-lobe shape for higher order harmonics. There is no higher order harmonic radiation in the direction of the laser propagation. In the backward direction, the distributions show an oscillatory pattern on θ and the number of peaks is equal to the number of harmonic order. Thus there is no even order harmonics to the direction of $\theta = 180^o$.

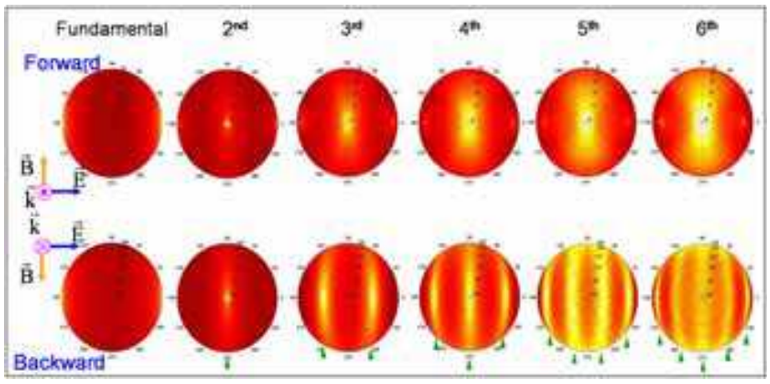

Fig. 7. Angular distributions of the RNTS harmonic radiations from an electron initially at rest. This was obtained with a linearly polarized laser pulse of 10^{18} W/cm^2 in intensity, 20 fs in FWHM pulse width. The green arrows in the backward direction indicate nodes.

For a laser intensity of 10^{20} W/cm^2 (a_o=6.4), the harmonic spectra from an electron initially at rest are plotted in Fig. 8 for different laser polarizations. In the case of a linearly polarized laser, the electron undergoes a zig-zag motion in a laser cycle. Thus the electron experiences severer instantaneous acceleration than in the case of a circularly polarized laser, in which case the electron undergoes a helical motion. This makes RNTS radiation stronger in intensity and higher in photon energy in the case of a linearly polarized laser. The most different characteristics are the appearance of a large-interval modulation in the case of a linear polarization denoted as '1' in Fig. 8 (a). This is also related with the zig-zag motion of the electron during a single laser cycle. During a single cycle, the electron's velocity becomes zero instantly, which does not happen in the case of the circular polarization. Thus a double peak radiation appears in a single laser cycle as shown in Fig. 9 (a). Such a double peak structure in the time domain makes the large-interval modulation in the energy spectrum. In

both cases, there are modulations with small-interval denoted by '2' in the Fig. 8 (a) and (b). This is caused by the variation of the laser intensity due to ultra-short laser pulse width. Such an intensity variation makes the drift velocity different for each cycle then the time interval between radiation peaks becomes different in time domain, which leads to a small-interval modulation in the energy spectrum.

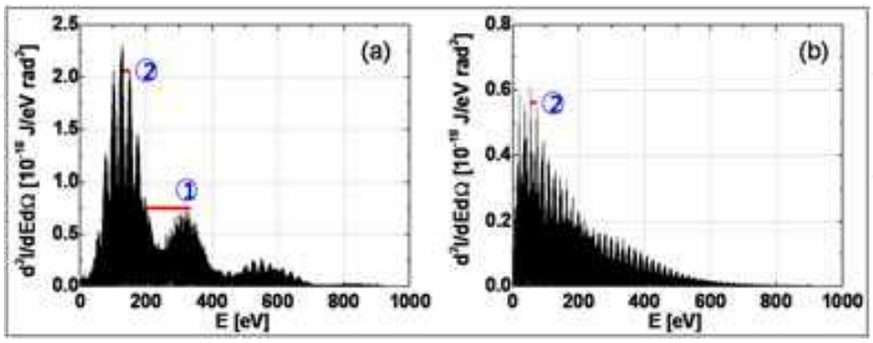

Fig. 8. RNTS spectra from an electron initially at rest on laser polarizations: (a) linear and (b) circular. The laser intensity of 10^{20} W/cm^2 (a_o=6.4) and the FWHM pulse width of 20 fs were used. Note that harmonic spectra are deeply modulated. See the text for the explanation.

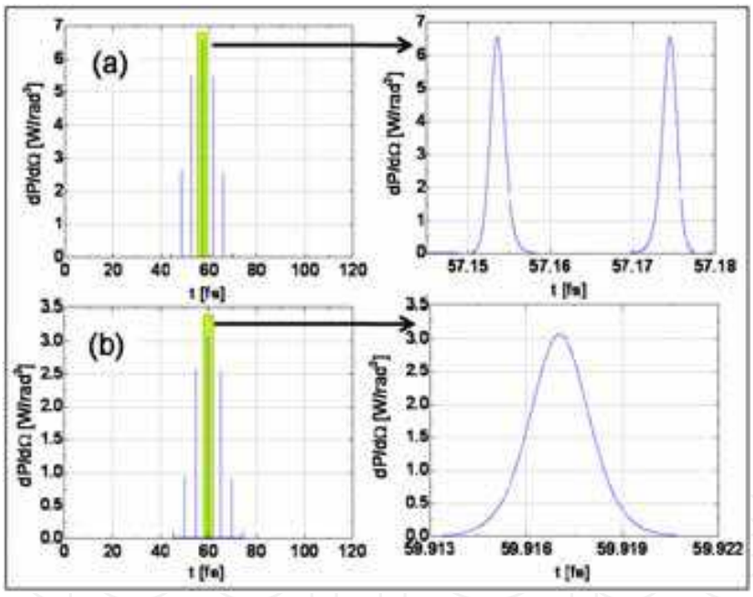

Fig. 9. Temporal shape of the RNTS radiations on polarizations with the same conditions as in Fig. 8: (a) linear and (b) circular polarization. The figures on the right hand side are the zoom-in of the marked regions in green color.

The temporal structure or the angular power can be seen in Fig. 9. As commented above, in the case of the linear-polarization, it shows a double-peak structure. One can also see that the pulse width of each peak is in the range of attosecond. This ultra-short nature of the RNTS radiation makes RNTS deserve a candidate for as an ultra-short intense high-energy photon source. The pulse width is proportional to the inverse of the band width of the harmonic spectrum, and thus scales on the laser intensity as $\sim a^{-3}$ (Lee et al., 2003b). The peak power is analytically estimated to scale $\sim a^5$ (Lee et al., 2003b).

The zig-zag motion of an electron under a linearly polarized laser pulse makes the radiation appears as a pin-like pattern in the forward direction as shown in Fig. 10 (a). However the radiation with a circularly polarized laser pulse shows a cone shape [Fig. 10 (b)] due to the helical motion of the electron. The direction of the peak radiation, θ_p was estimated to be $\theta_p \approx 2\sqrt{2} / a_o$ (Lee et al., 2006).

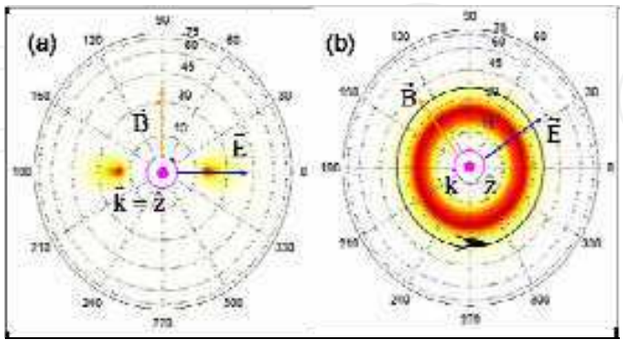

Fig. 10. Angular distributions of the RNTS radiations for different polarizations (a) linear and (b) circular polarization. The laser intensity of 10^{20} W/cm^2 (a_o=6.4) and the FWHM pulse width of 20 fs are used as in Fig. 8.

3. Coherent RNTS radiations

In the previous section, fundamental characteristics of the RNTS radiation are investigated in the case of single electron. It was also shown that the RNTS radiation can be an ultra-short radiation source in the range of attosecond. To maintain this ultra-short pulse width or wide harmonic spectrum even with a group of electrons, it is then required that the radiations from different electrons should be coherently added at a detector. In the case of RNTS radiation, which contains wide spectral width, such a requirement can be satisfied only if all the differences in the optical paths of the radiations from distributed electrons to a detector be almost the same. This condition can be practically restated: all the time intervals that scattered radiations from different electrons take to a detector, Δt_{int} should be comparable with or less than the pulse width of single electron radiation, Δt_{rad} as shown in Fig. 11. In the following subsections, two cases of distributed electrons, solid target and elelctron beam will be investigated for the coherent RNTS radiations.

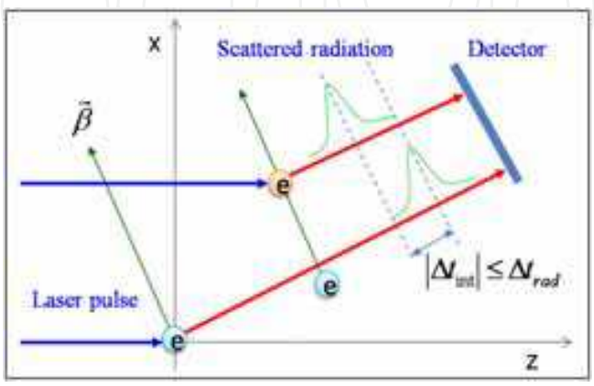

Fig. 11. Schematic diagram for the condition of coherent RNTS radiation.

3.1 Solid target

In the case of a solid target for distributed electrons (Lee et al, 2005), the time intervals that radiations take to a detector can be readily obtained with the following assumptions as the first order approximation: (1) plane wave of a laser field, (2) no Coulomb interaction between charged particles, thus neglecting ions, and (3) neglect of initial thermal velocity distribution of electrons during the laser pulse. With these assumptions, the radiation field $\vec{f}_i(t)$ by an electron initially at a position, $\vec{r}_i$, due to irradiation of an ultra-intense laser pulse propagating in the +z direction can be calculated from that of an electron initially at origin, $\vec{f}_o(t)$ by considering the time intervals between radiations from the electron at $\vec{r}_i$ and one at origin, Δt_i,

$$\Delta t_i = \Delta t'_i - \frac{\hat{n}\cdot\vec{r}}{c}, \tag{11}$$

where $\Delta t'_i = z_i / c$ is the time which the laser pulse takes to arrive at the i-th electron from origin: $\vec{f}_i(t) = \vec{f}_o(t - \Delta t_i)$. Then all the radiation fields from different electrons are summed on a detector to obtain a total radiation field, $\vec{F}(t)$ as

$$\vec{F}(t) = \sum_i \vec{f}_o(t - \Delta t_i). \tag{12}$$

The condition for a coherent superposition in the z-x plane can now be formulated by setting Eq. (11) to be less than or equal to the pulse width of single electron radiation, Δt_{rad}. This leads to the following condition [See Fig. 12]:

$$\left| z\tan\xi - x \right| \le \frac{c\Delta t_{rad}}{\sin(2\xi)}. \tag{13}$$

Equation (13) manifests that RNTS radiations are coherently added to the specular direction of an incident laser pulse off the target, if the target thickness, T_{hk} is restricted to

$$T_{hk} \le \frac{c\Delta t_{rad}}{\sin\xi}. \tag{14}$$

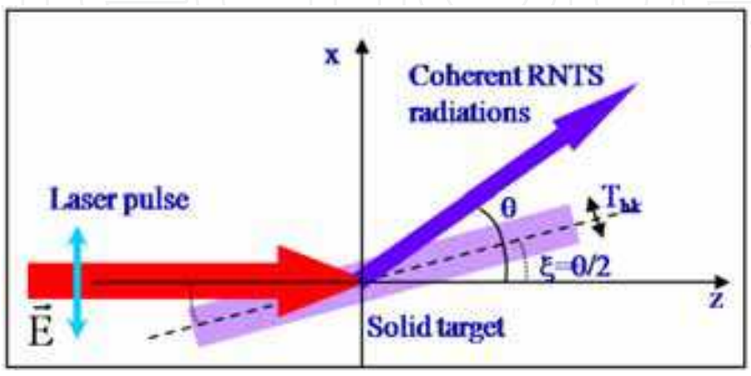

Fig. 12. Schematic diagram for a coherent RNTS condition with an ultrathin solid target.

Since the incident angle of the laser pulse can be set arbitrarily, one can set θ to the direction of the radiation peak of single electron, θ_p. For a linearly polarized laser with an intensity of 4x10^{19} W/cm^2, and a pulse duration of 20 fs FWHM, $\theta_p = 27^o$ and $\Delta t_{rad} = 5$ attosecond for a single electron. Equation (14) then indicates that the target thickness should be less than 7 nm. With these laser conditions, harmonic spectra were numerically obtained to demonstrates the derived coherent condition [Fig. 13].

The spectra in Fig. 13 (a) were obtained for a thick cylindrical target of 1 μm in thickness and radius, and 10^{18} cm^{-3} in electron density under the normal incidence of a laser on its base. The spectrum in Fig. 13 (b) is for the case of oblique incidence on an ultra-thin target of 7 nm in thickness, 5 μm in width, 20 μm in length, 10^{16} cm^{-3} in electron density, and $\xi = 13.5^o$, which were obtained with Eqs. (13) and (14). From Fig. 13 (b), which corresponds to the condition for coherent RNTS radiation, one can find that the spectrum from thin film (a group of electrons) has almost the same structure as that from a single electron radiation [Inset in Fig. 13 (b)] in terms of high-energy photon and a modulation. On the other hand, in the case of Fig. 13 (a), the harmonic spectra show much higher intensity at low energy part, which is caused by an incoherent summation of radiations.

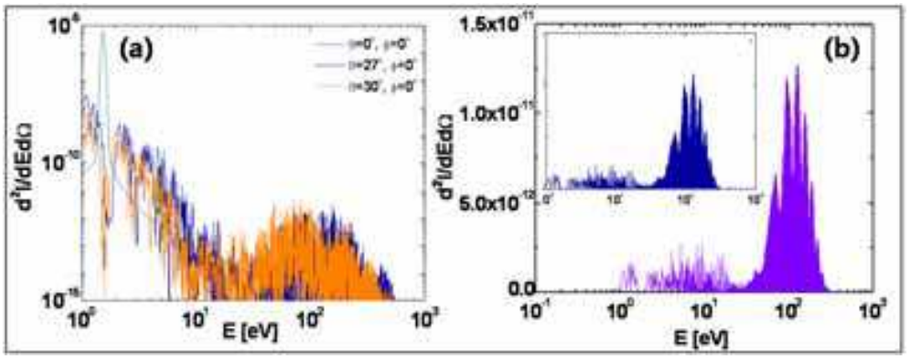

Fig. 13. RNTS spectra obtained under (a) incoherent and (b) coherent conditions. In (a), the spectra obtained in three different directions are plotted, while (b) were obtained in the specular direction. One can see that the spectrum in the coherent condition is very similar with that obtained from single electron calculation (inset of (b)).

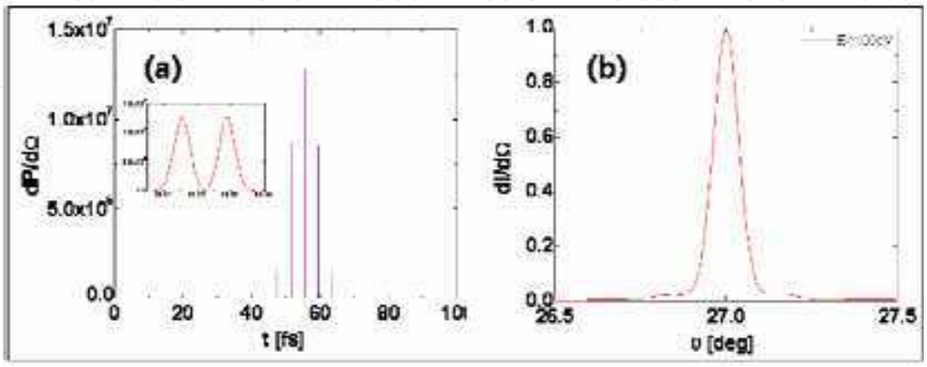

Fig. 14. (a) Temporal shape and (b) angular distribution in the case of the coherent condition [Fig. 13 (b)].

The temporal shape at the specular direction for the case of coherent condition [Fig. 13 (b)] is plotted in Fig. 14 (a), which shows an attosecond pulse. The direction-matched coherent condition also leads to a very narrow angular divergence as shown in Fig. 14 (b). It should be mentioned that with a thick cylinder target, the radiation peak appears at $\theta = 0^o$, because the dipole or fundamental radiation becomes dominant in that direction.

3.2 Electron beam

Exploiting a solid target for a coherent RNTS radiation may involve a complicated plasma dynamics due to an electrostatic field produced by a charge separation between electrons and ions. Instead, an idea using an electron beam has been proposed (Lee et al., 2006).

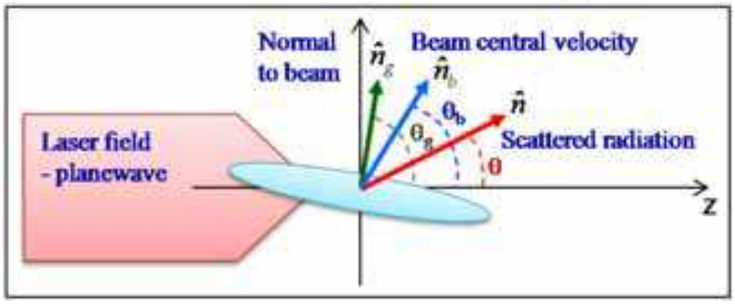

Fig. 15. Schematic diagram for the analysis of a coherent RNTS radiation with an electron beam.

Following similar procedure in the previous section, the RNTS harmonic spectrum can be obtained with that from an electron at center and its integration over initial electron distributions with phase relationships as

$$\vec{A}(\omega) \approx \vec{A}_c(\omega) \int dV_o f\left(\vec{r}_o, \vec{\beta}_o\right) \exp\left(i\delta \frac{\omega}{\omega_o}\right), \tag{15}$$

where $\vec{A}_c(\omega)$ is the angular spectral field from the central electron. The $\delta / k_o = \left(1 - \hat{n} \cdot \vec{\beta}_o\right) / \left(1 - \beta_{oz}\right) z - \hat{n} \cdot \vec{r}_o$ represents the phase relations between scattered radiations due to different initial conditions of the electrons. The distribution function can be assumed to have a Gaussian profile with cylindrical symmetry:

$$f\left(\vec{r}_o, \vec{\beta}_o\right) = \frac{N}{\left(2\pi\right)^3 R^2 L \sigma_\Gamma \sigma_{\beta'}^2} \exp\left[-\frac{x_o^{\,2} + y_o^{\,2}}{2R^2} - \frac{z_o^{\,2}}{2L^2}\right] \times \exp\left[-\frac{\beta_{ox}^2 + \beta_{oy}^2}{2\beta_b^2 \sigma_{\beta'}^2} - \frac{\left(\gamma_o - \gamma_b\right)^2}{2\gamma_b^2 \sigma_\Gamma^2}\right], \tag{16}$$

where the following parameters are used: the number of electrons (N), radius (R), length (L), fractional energy spread (σ_Γ), and divergence ($\sigma_{\beta'}$). γ_b is the relativistic gamma factor of the beam, and β_b its corresponding velocity divided by the speed of light. In the above formula, the beam velocity and the axis of the spatial distribution of the beam have the same directions and directed to +z, but below, the direction of the beam velocity ($\hat{n}_b$) and the axis of the beam ($\hat{n}_g$) are allowed to have different directions, as shown in Fig. 15. The integration of Eq. (15) by taking the first order of ($\vec{\beta}_b - \vec{\beta}_o$) in δ leads to the following formula for the coherent spectrum:

$$\vec{A}(\omega) \approx NF(\omega)\vec{A}_c(\omega), \tag{17}$$

$$F(\omega) \approx \frac{1}{\sqrt{1+k^2l^2}} \exp\left[-\frac{k^2}{2\left(1+k^2l^2\right)}\left(Q_r^2+Q_\beta^2\right)\right], \tag{18}$$

$$Q_r^2 = L^2N_{gz}^2 + R^2\left(N_{gx}^2+N_{gy}^2\right), \tag{19}$$

$$Q_\beta^2 = k^2R^2T^2\left[L^2\left(N_{gx}n_{gz}-N_{gz}n_{g\theta z}\right)^2 + N_{gy}^2\left(R^2n_{g\theta z}^2+L^2n_{gz}^2\right)\right], \tag{20}$$

with $k=\omega/c$ and the other parameters being

$$l^2 = T^2\left(L^2n_{gz}^2+R^2n_{g\theta z}^2\right), \tag{21}$$

$$T^2 = \left(\frac{\beta_b}{1-\beta_{bz}}\right)^2\left(\frac{\sigma_\Gamma^2}{\left(\gamma_b^2-1\right)^2}N_{bz}^2+\sigma_{\beta'}^2\left(N_{bx}^2+N_{by}^2\right)\right), \tag{22}$$

$$\vec{N}_s = \vec{M}_s\cdot\left(\hat{n}-p_b\hat{z}\right), \tag{23}$$

$$\vec{M}_s^T = \left[\hat{n}_{s\theta} \quad \hat{n}_{s\varphi} \quad \hat{n}_s\right], \tag{24}$$

$$p_b = \frac{1-\vec{\beta}_b\cdot\hat{n}_r}{1-\beta_{bz}}. \tag{25}$$

In Eqs. (23) and (24), the subscript, 's' represents either 'g' or 'b'. $\hat{n}_{s\theta}$ and $\hat{n}_{s\varphi}$ are two unit vectors perpendicular to $\hat{n}_s$. Equation (18) or the coherent factor, $F(\omega)$ shows that, as the beam parameters get larger, the coherent spectrum disappears from high frequency. This manifests that the phase matching condition among electrons is severer for high frequencies.

For the radiation scattered from an electron beam to be coherent up to a frequency ω_c, the above coherent factor $F(\omega)$, should be almost 1, or the exponent should be much smaller than 1 in the desired range of frequency. In the z-x plane, $N_{gy}=0$; then, this leads to the following relations, one for the angular relation:

$$N_{gx} = \sin\left(\theta-\theta_g\right)+\sin\theta_g\frac{1-\beta_b\cos\left(\theta_b-\theta\right)}{1-\beta_b\cos\theta_b} = 0, \tag{26}$$

and the other for the restriction on the electron beam parameters:

$$k_cLN_{gz}\sqrt{\frac{1+k_c^2R^2T^2\sin^2\theta_g}{1+k_c^2l^2}} < 1. \tag{27}$$

Eq. (26) also shows why the direction of the beam velocity (θ_b) is set to be different from the axis of the beam distribution (θ_g); otherwise, N_{gx} cannot be zero. The physical meaning of Eqs. (26) and (27) is that time delays between electrons should be less than the pulse width generated by a single electron as commented in the previous section. This equation can be used to find θ_g for given θ_b and θ which can be set to the optimal condition obtained from the single electron calculation. For the realization of the coherent condition, the most important things are the length of the electron beam (L) and the condition to minimize N_{gz}. To minimize N_{gz}, θ should be near 0o but not 0o at which only dipole radiation appears. From single electron calculation, it has been found that when $\theta_b \approx 0^o$ or in the case of a co-propagation (laser and electron beam propagate near the same direction), such a condition can be fulfilled.

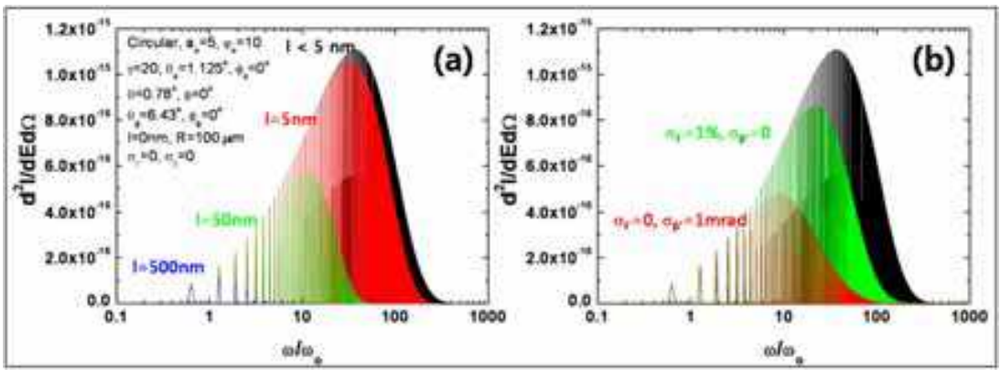

Fig. 16. Coherent RNTS radiation spectra for different beam parameters: (a) beam length and (b) other beam parameters. For better view, only envelops are plotted.

From the single electron calculation (the radiation from an electron of γ_o = 20 under irradiation of a circularly polarized laser of a_o = 5), it has been found that the peak radiation appears at $\theta = 0.78^o$ when $\theta_b = 1.125^o$. The insertion of these data into Eq. (26) and (27) leads to $\theta_g = 6.43^o$ and the beam length being restricted to a few nanometers. Coherent RNTS spectra for different electron beam parameters are plotted in Fig. 16. As expected, one can see that the coherent spectral intensity decreases at high frequencies as the beam length increases. These calculations show that the coherent conditions for the beam length and beam divergence are most stringent. However, with a moderate condition, the broadening of the coherent spectrum is still enough to generate about a 100-attosecond pulse.

4. Effects of the high-order laser fields under tight-focusing condition

Paraxial approximation is usually used to describe a laser beam. However, when the focal spot size gets comparable to the laser wavelength, it cannot be applied any more. This is the situation where the RNTS actually takes place. A tightly-focused laser field and its effects on the electron dynamics and the RNTS radiation will be discussed in this section.

4.1 Tightly focused laser field

The laser fields propagating in a vacuum are described by a wave equation. The wave equation can be evaluated in a series expansion with a diffraction angle, $\varepsilon = w_0 / z_r$, where w_0 is beam waist and z_r Rayleigh length. It leads to the following formulas for the laser

fields having linear polarization in the x-direction (zeroth-order) and propagating in the +z direction (Davis, 1979; Salamin, 2007),

$$E_x = E\left\{S_0 + \epsilon^2\left[\xi^2 S_2 - \frac{\rho^4 S_3}{4}\right] + \epsilon^4\left[\frac{S_2}{8} - \frac{\rho^2 S_3}{4} - \frac{\rho^2(\rho^2 - 16\xi^2)S_4}{16} - \frac{\rho^4(\rho^2 + 2\xi^2)S_5}{8} + \frac{\rho^8 S_6}{32}\right]\right\}, \quad (28)$$

$$E_y = E\xi\upsilon\left\{\epsilon^2[S_2] + \epsilon^4\left[\rho^2 S_4 - \frac{\rho^4 S_5}{4}\right]\right\}, \quad (29)$$

$$E_z = E\xi\left\{\epsilon[C_1] + \epsilon^3\left[-\frac{C_2}{2} + \rho^2 C_3 - \frac{\rho^4 C_4}{4}\right] + \epsilon^5\left[-\frac{3C_3}{8} - \frac{3\rho^2 C_4}{8} + \frac{17\rho^4 C_5}{16} - \frac{3\rho^6 C_6}{8} + \frac{\rho^8 C_7}{32}\right]\right\}, \quad (30)$$

$$B_x = 0, \quad (31)$$

$$B_y = E\left\{S_0 + \epsilon^2\left[\frac{\rho^2 S_2}{2} - \frac{\rho^4 S_3}{4}\right] + \epsilon^4\left[-\frac{S_2}{8} + \frac{\rho^2 S_3}{4} + \frac{5\rho^4 S_4}{16} - \frac{\rho^6 S_5}{4} + \frac{\rho^8 S_6}{32}\right]\right\}, \quad (32)$$

$$B_z = E\upsilon\left\{\epsilon[C_1] + \epsilon^3\left[\frac{C_2}{2} + \frac{\rho^2 C_3}{2} - \frac{\rho^4 C_4}{4}\right] + \epsilon^5\left[\frac{3C_3}{8} + \frac{3\rho^2 C_4}{8} + \frac{3\rho^4 C_5}{16} - \frac{\rho^6 C_6}{4} + \frac{\rho^8 C_7}{32}\right]\right\}. \quad (33)$$

The laser fields are written up to the 5th order in ε. In above equations, $E = E_o(w/w_o)g(t - z/c)\exp(-r^2/w^2)$, $w = w_0\sqrt{1 + (z/z_r)^2}$, $z_r = \pi w_0^2/\lambda$, $\xi = x/w_0$, $\upsilon = y/w_0$, $\zeta = z/z_r$, and $\rho^2 = \xi^2 + \upsilon^2$. $g(t - z/c)$ is a laser envelop function. C_n and S_n are defined as

$$C_n = \left(\frac{w_0}{w}\right)^n \cos(\psi + n\psi_G); \qquad n = 0,1,2,3\ldots,$$
$$S_n = \left(\frac{w_0}{w}\right)^n \sin(\psi + n\psi_G), \quad . \quad (34)$$

where $\psi = \psi_0 + \omega t - kz - kr^2/2R + \psi_G$ and $R = z + z_r^2/z$. ψ_0 is a constant initial phase and k is the laser wave number, $2\pi/\lambda$. ψ_G is the Gouy phase expressed as

$$\psi_G = \tan^{-1}\frac{z}{z_r}. \quad (35)$$

The zeroth order term in ε is a well known Gaussian field. One can see when ε cannot be neglected: when the focal size gets comparable to the laser wavelength, a field longitudinal to the propagation direction appears and the symmetry between the electric and the magnetic fields is broken.

Because ε is proportional to $1/w_0$, the high order fields (HOFs) become larger for smaller beam waist. Figure 17 shows that E_y and E_z get stronger as w_o decreases. The peak field strengths of E_y and E_z amount to 2.6% and 15% of E_x at w_o = 1 μm, respectively. In the case of a counter-interaction between an electron and a laser pulse, HOFs much weaker than the zeroth-order field does not affect the electron dynamics. However, when the relativitic electron is driven by a co-propagating laser pulse, weak HOFs significantly affect the electron dynamics and consequently the RNTS radiation.

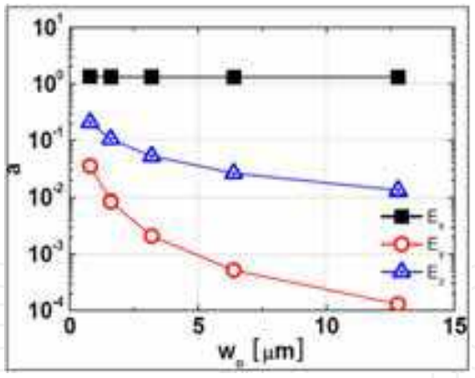

Fig. 17. The strength of laser electric fields against the beam waist size are plotted in unit of the normalized vector potential. The laser field is evaluated at ($w_0/2$, $w_0/2$, 0) with the zeroth-order laser intensity of $a_0 = 2.2$.

4.2 Dynamics of an electron electron with a tightly focused laser

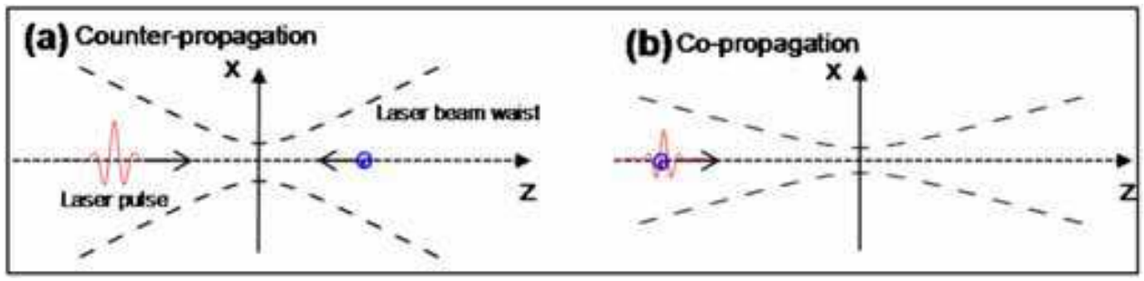

Fig. 18. Two interaction schemes between a relativistic electron and a laser pulse:
(a) counter-propagation and (b) co-propagation.

The dynamics of a relativistic electron under a tightly-focused laser beam is investigated by the Lorentz force equation [Eq. (1)]. One can consider two extreme cases of interaction geometry as shown in Fig. 18. The counter-propagation scheme, or Compton back-scattering scheme is usually adopted to generate monochromatic x-rays. It has been shown in the previous section that the co-propagation scheme is more appropriate to generate the coherent RNTS radiation. For such schemes, the effect of HOFs will be investigated.

In the z-x plane, $E_y = B_z = 0$, then the Lorentz force equation for γ and β_x (transverse velocity) in the case of the counter-propagation scheme ($\vec{\beta} \approx -1\hat{z}$), can be approximated as,

$$\frac{d\gamma}{d\tau} \approx a_0 \beta_x - a_{odd}^H , \tag{36}$$

$$\frac{d(\gamma\beta_x)}{d\tau} \approx 2a_0 + \left(a_{even}^H + b_{even}^H\right), \tag{37}$$

where $\tau = \omega_L t$, a_0 is the zeroth-order laser field in unit of the normalized potential. a_{odd}^H is odd HOFs of electric field (or longitudinal electric fields). a_{even}^H and b_{even}^H are even HOFs of electric and magnetic fields, respectively [see Eqs. (28)-(33)]. From above equations, γ can be analytically obtained considering only the first HOF as

$$\frac{\gamma}{\gamma_o} \approx 1 + \eta_o^2 - \frac{\alpha_1}{2\gamma_o^2}\left(1 - \eta_o^2\right), \tag{38}$$

where $\eta_o^2 = \left(1 + \alpha_0^2\right) / 2\gamma_0^2$ and α_1 is the integration of the first-order electric field over phase. For a highly relativistic electron or $\gamma_o >> 1$, the above equations show that the HOFs contribute to the electron dynamics just as a small correction to the zeroth-order field. Figure 19 (a) shows the time derivatives of the gamma factor and the transverse velocity. It is hardly to notice any change due to HOFs.

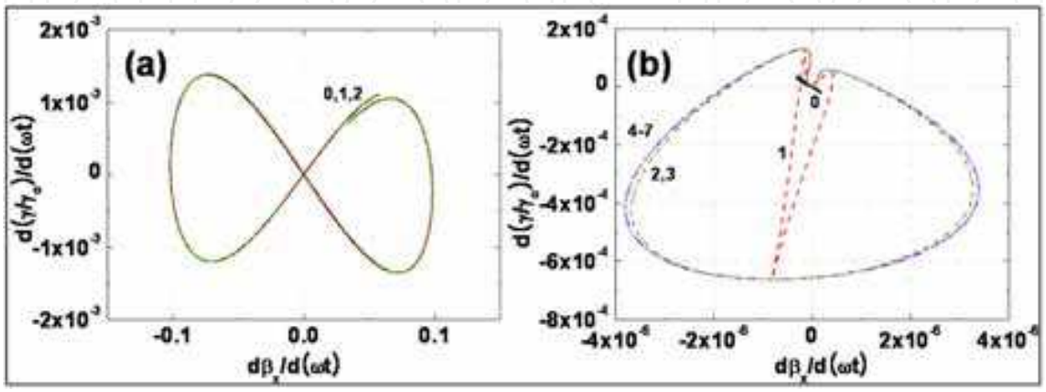

Fig. 19. Variation of the time derivatives of the relativsitic gamma factor and the transverse velocity for (a) counter-propagation and (b) co-propagation schemes. In this calculation, the laser pulse with λ = 0.8 μm, w_o = 4 μm, a_o = 10, and Δt_{FWHM} = 5 fs interacts with an electron with E_o = 100 MeV. The numbers in the figures indicate up to which order HOFs are included.

However, when the electron co-propagates with the laser pulse ($\vec{\beta} \approx +1\hat{z}$), the situation dramatically changes. The Lorentz force equations are

$$\frac{d\gamma}{d\tau} \approx a_0 \beta_x + a_{odd}^H, \tag{39}$$

$$\frac{d\left(\gamma\beta_x\right)}{d\tau} \approx \frac{a_0}{2\gamma^2} + \left(a_{even}^H - b_{even}^H\right). \tag{40}$$

The relativistic gamma factor is given by

$$\frac{\gamma}{\gamma_o} \approx \frac{1 + \alpha_0^2}{1 - 2\gamma_o \alpha_1}. \tag{41}$$

Now the change of the gamma factor becomes significant and γ gets even smaller than its initial value. This cannot happen in the counter-propagation scheme [Eq. (38)]. The acceleration in the transverse direction can be dominated by the HOFs when $a_0 / \gamma^2 << 1$. This section deals with this kind of case, where $a_0 \le 10$ and $\gamma_0 >> 10$. As expected, Figure 19 (b) shows that the time derivative of the gamma factor increases with inclusion of the first order HOF and that of the transverse velocity is significantly enhanced with the inclusion of the second-order HOF. Even though the zeroth order field is much stronger than the HOFs,

the high gamma factor makes it negligible compared with the HOFs. It is the difference between the high order electric and the magnetic fields that contributes to such a dramatic change in the dynamics. Higher order fields than the second order just contributes to the dynamics as a small correction in this case (In some special cases where the spatial distribution of HOFs gets important near axis, they can be more considerable.). It is also interesting to note that the scaling of the transverse acceleration on the gamma factor changes from $\propto \gamma_0^{-3}$ to $\propto \gamma_0^{-1}$ due to the inclusion of the second-order field.

4.3 Radiation from a co-propagating electron with a tightly focused laser

As shown in Sec. 2, nonlinear motion of an electron contributes to the harmonic spectra, or ultra-short pulse radiation. Thus it can be inferred that the enhancement of nonlinear dynamics with inclusion of HOFs, increase of gamma factor (or electron energy variation) by the first order field and the transverse acceleration by the second-order field, might enhance the RNTS radiations.

Figure 20 shows the effect on RNTS as HOFs are included. Figure 20 is the RNTS radiation obtained from the dynamics in Fig. 19 (b). The number on the plot is the number of order of HOF, up to which HOFs are included. Note that as the HOFs are included, the pulse duration gets shorter and the spectrum gets broader according. The radiation intensity is also greatly enhanced. It should be notices that it is the transverse acceleration that significantly enhances the RNTS radiations. Figure 20 shows the shorter pulse width or wider spectral width by a factor of more than 5 and the higher intensity by an order of magnitude.

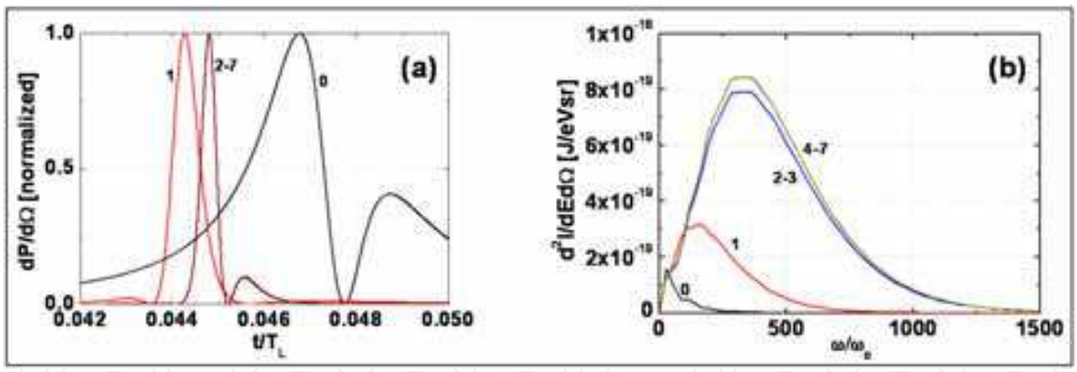

Fig. 20. (a) The normalized temporal structure of the radiation from the dynamics presented in Fig. 19 (b). Each radiation is plotted in the direction of the maximum radiation, which is -0.03° and -0.16° for zeroth-order and first-order, respectively and converges to -0.12° for higher orders. The peak powers for each plot are 2.1, 77, and 580 W/rad2. (b) The harmonic spectrum for the same case.

In the tight-focusing scheme, the strong radiation can be assumed to be generated within the focal region. That is, the electron radiates when it passes through Rayleigh range approximately in length scale, or $\Delta t' = 2z_r / \beta c$ in the electron's own time. Then for $\beta \approx 1$, the period in the detector's own time, Δt can be approximately obtained as

$$\Delta t \approx \frac{2z_r(1-\beta)}{c\beta} \approx \frac{z_r}{c\gamma^2} = \frac{\pi}{c\lambda}\frac{w_0^2}{\gamma^2}. \tag{42}$$

The average photon energy can be approximated to the mean photon energy and then it can be estimated from the inverse of the pulse width according to the Fourier transform as

$$E_{av} \approx \frac{E_{\max} + E_{\min}}{2} \approx \frac{E_{\max}}{2} \approx \frac{\hbar \Delta\omega}{2} \propto \frac{1}{\Delta t} \propto \frac{\gamma^2}{w_o^2} . \tag{43}$$

This shows that the average photon energy scales inversely with the square of the beam waist, as also shown later. The total radiation power, radiated power integrated over whole angle, from an accelerated electron is described as (Jackson, 1999)

$$P(t') = \frac{2}{3}\frac{e^2}{c}\gamma^6[(\dot{\vec{\beta}})^2 - (\vec{\beta} \times \dot{\vec{\beta}})^2] . \tag{44}$$

The radiated powers in the electron's own time (retarded time) $P(t')$ and in the detector's own time $P(t)$ are related to each other by the relation of $P(t) = P(t')(dt'/dt) = P(t')/(1 - \hat{n} \cdot \vec{\beta})$ [Eq. (11)]. When $|\vec{\beta}| \approx 1$ and $\hat{n}$ is almost parallel to $\vec{\beta}$, $(1 - \hat{n} \cdot \vec{\beta})$ can be approximated to $1/(2\gamma^2)$, which leads to $P(t) \approx 2\gamma^2 P(t')$. When $\dot{\vec{\beta}}$ is parallel to $\vec{\beta}$, the radiated power integrated over all the angles is given by

$$P_{||}(t) = \frac{4}{3}\frac{e^2}{c}\gamma^8 \dot{\beta}_{||}^2 . \tag{45}$$

On the other hand, when $\dot{\vec{\beta}}$ is perpendicular to $\vec{\beta}$ the radiation power is expressed as

$$P_{\perp}(t) = \frac{4}{3}\frac{e^2}{c}\gamma^6 \dot{\beta}_{\perp}^2 . \tag{46}$$

$\dot{\vec{\beta}}$ can be obtained from the Lorentz force equation [Eq. (1)]. The acceleration term $d(\gamma\vec{\beta})/dt$ can be expanded as $\gamma\dot{\vec{\beta}} + \dot{\gamma}\vec{\beta}$. The first term contributes to $P_{\perp}$, while the second term to $P_{||}$. From this relation, the $\dot{\beta}$ can be expressed with an effective field $\vec{F} = \vec{E} + \vec{\beta} \times \vec{B}$ and γ. Then Eqs. (45) and (46) can be re-written as

$$P_{||}(t) \cong \frac{4}{3}\frac{e^4}{mc^3}\gamma^8 \left|\frac{\vec{F}_{||}}{\beta^2\gamma^3}\right|^2 \cong \frac{4}{3}\frac{e^4}{mc^3}\gamma^2 |\vec{F}_{||}|^2 \tag{47}$$

and

$$P_{\perp}(t) \cong \frac{4}{3}\frac{e^4}{mc^3}\gamma^6 \left|\frac{\vec{F}_{\perp}}{\gamma}\right|^2 = \frac{4}{3}\frac{e^4}{mc^3}\gamma^4 |\vec{F}_{\perp}|^2 , \tag{48}$$

respectively. The effective fields for different harmonic orders can be approximated as

$$\vec{F}_{(0)} = ES_1(1 - \beta)\hat{x} \cong \frac{ES_1}{2\gamma^2}\hat{x} . \tag{49}$$

$$\vec{F}_{(1)} = E\xi\varepsilon\left[C_2\right]\hat{z}\,. \tag{50}$$

$$\vec{F}_{(2)} = E\varepsilon^2\left\{-(1-\beta)\frac{\rho^4 S_4}{4} + \left[\xi^2 - \frac{\rho^2}{2}\beta\right]S_3\right\}\hat{x} \cong E\varepsilon^2 S_3\left[\xi^2 - \frac{\rho^2}{2}\beta\right]\hat{x}\,. \tag{51}$$

Then the total radiation energy can be calculated by the multiplication of the pulse width and the power. Using the estimated Δt of Eq. (42), the total radiation energy of single electron, I, can be estimated from Eqs. (47) and (48) as follows:

$$I_{||} \propto w_0^2 \,|\vec{F}_{||}|^2\,. \tag{52}$$

$$I_{\perp} \propto w_0^2\gamma^2 \,|\vec{F}_{\perp}|^2\,. \tag{53}$$

With the effective fields [Eqs. (49)-(51)] and the radiation energy relations of Eqs. (47) and (48), the radiation energy for the field of certain order is evaluated as follows:

$$I_{(0)} \propto \varepsilon^0\gamma^{-2}\,. \tag{54}$$

$$I_{(1)} \propto \varepsilon^1\gamma^0\,. \tag{55}$$

$$I_{(2)} \propto \varepsilon^2\gamma^2\,. \tag{56}$$

The effective strength of the zeroth-order field is much smaller than those of HOFs because $1/\varepsilon$ is only ~20 and much smaller than γ^2 ($\gamma^2 > 10000$ in the current study). From this, one can see that the magnitudes of the radiation energies can be ordered as $I_{(0)} << I_{(1)} << I_{(2)}$. Since the transverse field is more effective than the longitudinal field for scattering radiation, $I_{(1)}$ is smaller than $I_{(2)}$. The HOFs higher than the second-order do not make significant contribution to radiation; they can be just considered as a small correction.

5. Generation of an intense attosecond x-ray pulse

In the case of the interaction of an electron bunch with a laser, there are three major interaction geometries: counter-propagation (Compton backscattering), 90°-scattering, and co-propagation (0°-scattering) geometry. To estimate the pulse width of the radiation in these interaction geometries, we need to specify the length (L_{el}) and diameter (L_T) of the electron bunch, the pulse length (L_{laser}) of the driving laser and the interaction length (confocal parameter, L_{conf}). At current technology, the diameter of an electron bunch is typically 30 μm. The typical pulse widths of an relativistic electron bunch (v~c) and femtosecond high power laser are about 20 ps and 30 fs, respectively, which corresponds to L_{el}~ 6 mm and L_{laser} ~ 9 μm in length scale. For the beam waist of 5 μm at focus, the confocal parameter is L_{conf} ~ 180 μm for 800 nm laser wavelength. In other words, $L_e >> L_{conf} >> L_{laser}$ are rather easily satisfied. In the following, we confine our simulation to this case. In this situation, the radiation pulse width is then roughly estimated to be $\Delta t_{counter} \sim 2L_{conf}/c$=600 fs, $\Delta t_{90} \sim (L_T+L_{laser})/c$=130 fs, and $\Delta t_{co} \sim L_{laser}/c$=5 fs, for counter-propagation, 90°-scattering, and co-propagation geometry, respectively. When we consider the aspect of the x-ray pulse duration, the co-propagation geometry is considered to be adequate as an interaction geometry.

The co-propagating interactions between a femtosecond laser pulse and an electron bunch were demonstrated as series of simulations. The simulations are similar to those in Section 4. The difference is that the electron bunch and the pulsed laser, co-propagating along the +z direction, meet each other in the center of the tightly focused region (z = 0). The interaction between electrons is ignored because it is much weaker than the interaction between the laser field and electrons.

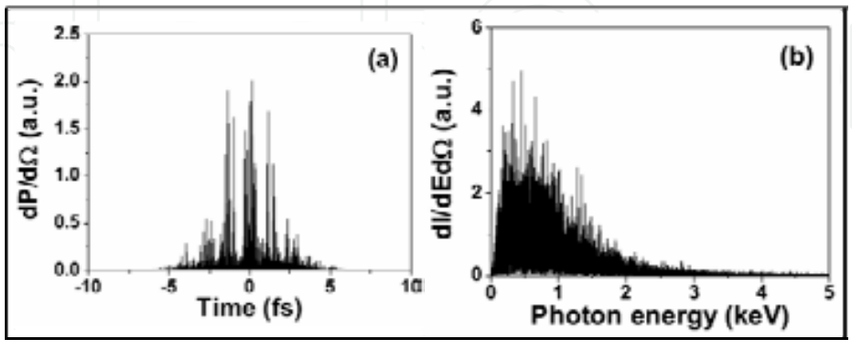

Fig. 21. (a) Temporal structure and (b) spectrum of the radiation from the co-propagation interaction between a 5 fs FWHM laser with 5 μm beam waist and an electron bunch of 200 MeV energy. The laser intensity at focus is 2.1 × 10^{20} W/cm² (a_0 = 10).

Figure 21 shows the temporal structure and the spectrum of the radiation from the interaction between an electron bunch and a co-propagating tightly focused fs laser. The pulse width and the wavelength of the laser is 5 fs FWHM and 800 nm (1.55 eV), respectively. The laser is focused to a beam waist of 5 μm at z=0 with an intensity of 2.1x10^{20} W/cm² ($a_0 = 10$). The electron bunch has a radius of 30 μm and a length of 30 μm (or a pulse of 100 fs) and a normalized emittance of 2 mm mrad. The energy of the electron bunch is 200 MeV and the energy spread is 0.1 %. The electron bunch consists of 3.0×10^4 electrons which are randomly sampled with the Gaussian distribution [Eq. 16)] throughout the bunch. The both centers of the electron bunch and the laser meet at the center of the focus (z=0). The radiation is detected at the angle of $\theta = 0$. Figure 21 (a) shows that the width of the X-ray pulse radiated from the electron bunch is about 5 fs, which is the same as that of the laser pulse, as mentioned in the above. The spectrum [Fig.21(b)] shows that very high-energy photons are produced as mentioned in previous section.

Figure 22 shows the total radiated energy and the averaged photon energy. The calculations have been done for various electron energies. To check the effect of the HOFs, the simulation have been carried out for various combinations of high order fields: (1) the zeroth-order only, up to (2) the first-, (3) the second-, and (4) the seventh-order fields. The electron bunch consists of 7.5×10^3 electrons. The total radiated energy has been obtained by the integration of the angular radiation energy over the angle $\theta = 1/\gamma$. The conditions are the same as those of Fig. 21, unless otherwise mentioned. Each point of data is the average of the four sets of simulations. The standard deviations are always smaller than 5 % and the error bars are omitted because they are not visible in the log scale.

Figure 22 (a) also shows the γ dependence of the total radiated energies $I_{(0)}$, $I_{(0,1)}$, $I_{(0-2)}$ and $I_{(0-7)}$. The fitting to the simulation data shows $I_{(0)} \propto \gamma^{-2.03}$ which is a good agreement

with Eq. (53). In case of $I_{(0,1)}$ which includes both the zeroth- and the first-order field, the first-order field mainly contributes to the radiation and the total radiated energy $I_{(0,1)}$ is independent of γ as Eq. (54). $I_{(0-2)}$, which contains the fields up to the second-order, is proportional to $\gamma^{+1.94}$, indicating that its behaviour is dominated by the second-order field, as Eq. (55). $I_{(0-7)}$ is almost the same as $I_{(0-2)}$, implying that the fields higher than the second-order make a negligible contribution.

The study about an electron acceleration using a tightly-focused laser field by Salamin et al. showed that at least the fields up to the fifth-order are required to describe correctly the dynamics of an electron (Salamin & Keitel, 2002). In that calculation, a low energy ($\gamma < 24$) electron was injected to a focused region at a finite angle ($5^\circ < \theta < 12^\circ$) with respect to the laser propagation. Even though the fields higher than the third-order are small, HOFs can still deflect the path of such a low energy electron. Because the strength of HOfs is sensitive to the position in the case of a tight focus, the interaction dynamics can be different with a low energy electron. However, for a high energy electron ($\gamma > 100$), which is effectively heavy, the deflection of the electron's path by HOFs can be neglected.

As expected in Eq. (43), the average photon energy of the radiation is also proportional to γ^2 as manifested in Fig. 22 (b). Figure 22 (c) shows the dependence of the radiated photon energy on beam waist when the energy of electron is 1 GeV and the radius of the electron bunch 30 μm (the laser parameters are the same as before). HOFs up to the seventh-order were included. It shows that the average photon energy is proportional to w_0^{-2} as expected in Eq. (43). Hence the photon energy is tunable by changing the beam waist as well as the electron energy. The average photon energy is 38 keV for an electron energy of 2 GeV, but higher photon energy is expected for higher electron energy. As mentioned in the introduction it can fill the region shorter than 5 fs and higher than 10 keV of Fig. 2.

Because both of the photon energy E and the total radiated energy I is proportional to γ^2, the number of the radiated photons I/E is independent of γ. For an electron bunch of 1 nC charge, $a_0 = 10$, $w_0 = 5$ μm and the pulse width of 5 fs FWHM, the number of radiated photon is 4.2×10^6. For the counter-propagation interaction (180° collision) between the same electron bunch and laser pulse, the number of the radiated photons is 1.2×10^8 (Hartemann et al., 2005). The radiated photon number in the co-propagation interaction is only 30 times less than the 180° collision when HOfs are taken into account.

This represents a remarkable enhancement if we notice that when only the zeroth-order field is considered, the photon numbers in the co-propagation interaction are 3×10^3 and 3×10^7 times less than those in the counter-propagation interaction, for an electron energy of 50 MeV and 1 GeV, respectively. In terms of the photon number per unit time, both interaction geometry are comparable because the radiation pulse width from co-propagation interaction (< 5 fs) is ~20 times smaller than that from 180° collision (> 100 fs).

The study also shows that the radiation efficiency of an electron increases as the focal spot gets smaller. The radiation efficiency can be defined by the radiated energy divided by both the number of the electron effectively participating in the radiation N_{eff} and the energy of the driving laser I_L:($I/N_{eff} \cdot I_L$). Figure 23 shows the radiation efficiency of an electron with respect to the change of the beam waist. For fair comparison, the laser intensity is kept constant for different beam waists (a_0 = 10 for all the data in Fig. 23). It is shown that the efficiency scales inversely to the 4th power of the beam waist. This scaling can be understood

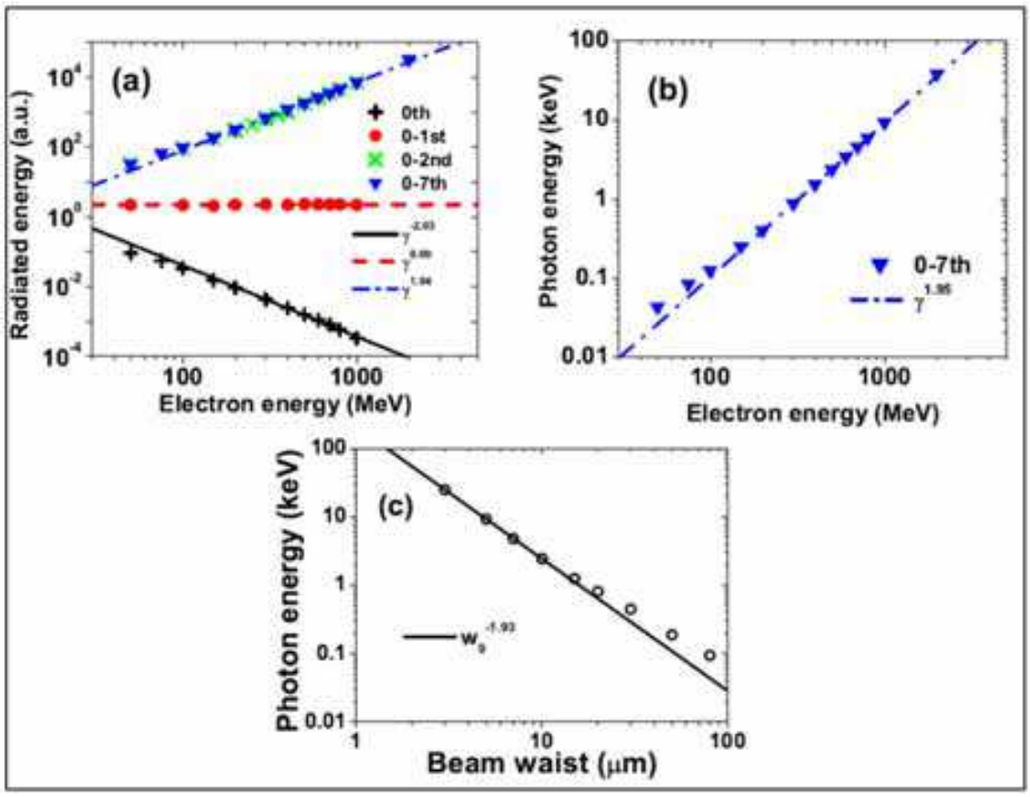

Fig. 22. Dependence of (a) the total radiated energy I and (b) the average photon energy E on γ. The effect of high-order fields in ε is also shown in (a) for different combination of high-order fields. (c) The dependence of the average photon energy on w_0. The normalized vector potential of the laser a_0 is 10, beam waist of laser w_0=5 μm and radius of the electron bunch 30 μm.

as follows: The radius of the electron bunch is assumed to be much larger and the electrons are uniformly distributed so that the electron number participating in the radiation N_{eff} is proportional to the square of the laser beam waist. As explained previously, the total radiated energy from a single electron, $I_{(0-7)} \cong I_{(2)} \propto \varepsilon^2\gamma^2 \propto w_0^{-2}$. Because the laser intensity is kept constant, the energy of the driving laser is then proportional to w_0^2. Hence, $I/(I_L N_{eff})$ is proportional to the w_0^{-4} as shown in Fig. 23. If the density of the electron is constant and the radius of the electron bunch is much larger than the beam waist, the number of electrons participating in the radiation is proportional to w_0^2 and the radiated energy per laser energy, I/I_L is proportional to w_0^{-2}. In a real electron bunch the electron density is not uniform but larger at the center than in the outer part, thus I/I_L decreases more rapidly than w_0^{-2}. In other words, the smaller focal spot size is preferred to the larger one for higher flux of photons for the same laser intensity because the radiation efficiency of electron is higher and the laser energy needed is less. Note in Fig. 23 that the slope changes near the beam waist of 20 μm. It is because the contribution from HOFs (mainly the 2nd order) decreases as the beam waist increases.

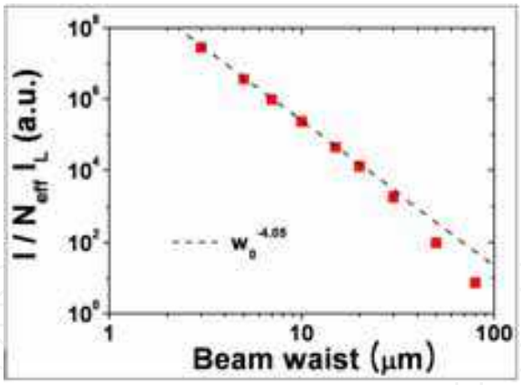

Fig. 23. Change of the radiation efficiency with respect to the beam waist. The radiation efficiency is here defined by the radiation energy I divided by the number of the electrons effectively participating in the radiation N_{eff} and the energy of the driving laser I_L : $I/(I_L N_{eff})$ the laser intensity is kept constant ($a_0 = 10$) for different beam waists.

6. References

Afonso, C. N.; Solis, J.; Catalina, F.; & Kalpouzos, C. (1996). Existence of Electronic Excitation Enhanced Crystallization in GeSb Amorphous Thin Films upon Ultrashort Laser Pulse Irradiation, *Appl. Phys. Lett.*, Vol. 76, 2519-2522, ISSN 0003-6951

Banerjee, S.; Valenzuela, A. R.; Shah, R. C.; Maksimchuk, A. & Umstadter, D. (2002). High harmonic generation in relativistic laser–plasma interaction, *Phys. Plasmas*, Vol. 9, 2393-2398, ISSN 1070-664X

Beaud, P.; Johnson, S. L.; Streun, A.; Abela, R.; Abramsohn, D.; Grolimund, D.; Krasniqi, F.; Schmidt, T.; Schlott, V. & Ingold, G. (2007). Spatiotemporal Stability of a Femtosecond Hard–X-Ray Undulator Source Studied by Control of Coherent Optical Phonons, *Phys. Rev. Lett.*, Vol. 99, 174801-1-4, ISSN 0031-9007

Bloembergen, N. (1999). From nanosecond to femtosecond, science, *Rev. of Mod. Phys.*, Vol. 71, S283-S287, ISSN 0034-6861

Brown, L. S. & Kibble, T. W. B. (1964). Interaction of Intense Laser Beams with Electrons, *Phys. Rev.*, Vol. 133, A705-A719, ISSN

Cavalieri, A.; Müller, L. N.; Uphues, Th.; Yakovlev, V. S.; Baltuška, A.; Horvath, B.; Schmidt, B.; Blümel, L.; Holzwarth, R.; Hendel, S.; Drescher, M.; Kleineberg, U.; Echenique, P. M.; Kienberger, R.; Krausz , F. & Heinzmann, U. (2007). Attosecond spectroscopy in condensed matter, *Nature*, Vol. 449, 1029-1032, ISSN 0028-0836

Chen, S.-Y.; Maksimchuk, A. & Umstadter, D. (1998). Experimental observation of relativistic nonlinear Thomson scattering, *Nature*, Vol. 396, 653-655, ISSN 0028-0836

Chen, S.-Y.; Maksimchuk, A.; Esarey, E. & Umstadter, D. (2000). Observation of Phase-Matched Relativistic Harmonic Generation, *Phys. Rev. Lett.*, Vol. 84, 5528-5531, ISSN 0031-9007

Chung, S-Y.; Yoon, M-H. & Kim, D-E. (2009). Generation of Attosecond X-ray and gamma-ray via Compton backscattering, *Optics Express*, Vol. 17, 7853-7861, ISSN 1094-4087

Davis, L. W. (1979). Theory of electromagnetic beams, *Phys. Rev. A*, Vol. 19, 1177-1179, ISSN 1050-2947

Drescher, M.; Hentschel, M.; Kienberger, R.; Uiberacker, M.; Yakovlev, V.; Scrinzi, A.; Westerwalbesloh, Th.; Kleineberg, U.; Heinzmann, U. & Krausz, F. (2002). Time-resolved atomic inner-shell spectroscopy, *Nature*, Vol. 419, 803-807, ISSN 0028-0836

Esarey, E. & Sprangle, P. (1992). Generation of stimulated backscattered harmonic radiation from intense-laser interactions with beams and plasmas, *Phys. Rev. A*, Vol. 45, 5872-5882, ISSN 1050-2947

Esarey, E.; Ride, S. K. & Sprangle, P. (1993a). Nonlinear Thomson scattering of intense laser pulses from beams and plasmas, *Phys. Rev. E*, Vol. 48, 3003-3021, ISSN 1539-3755

Esarey, E.; Ting, A.; Sprangle, P.; Umstadter, D. & Liu, X. (1993b). Nonlinear analysis of relativistic harmonic generation by intense lasers in plasmas, *IEEE Trans. Plasma Sci.*, Vol. 21, 95-104, ISSN 0093-3813

Fleming, G. & Ratner, M. (2008). Grand challenges in basic energy, sciences, *Physics Today*, July, Vol. 28, 8-80, ISSN

Gaffney, K. J. & Chapman, H. N. (2008). Imaging Atomic Structure and Dynamics with Ultrafast X-ray Scattering, *Science*, Vol. 316, 1444-1448, ISSN 0036-8075

Gai, F.; Hasson, K.; McDonald, C. J. C. & Anfinrud, P. A. (1998). Chemical Dynamics in Proteins: The Photoisomerization of Retinal in Bacteriorhodopsin, *Science*, Vol. 279, 1886-1891, ISSN 0036-8075

Girolami, B.; Larsson, B.; Preger, M.; Schaerf, C. & Stepanek, J. (1996). Photon beams for radiosurgery produced by laser Compton backscattering from relativistic electrons, *Phys. Med. Biol.*, Vol. 41, 1581-1596, ISSN 0031-9155

Goulielmakis, E.; Schultze, M.; Hofstetter, M.; Yakovlev, V. S.; Gagnon, J.; Uiberacker, M.; Aquila, A. L.; Gullikson, E. M.; Attwood, D. T.; Kienberger, R.; Krausz, F. & Kleineberg, U. (2008). Single-cycle nonlinear optics, *Science*, Vol. 320, 1614-1617, ISSN 0036-8075

Harris, S. E. & Sokolov, A. V. (1998). Subfemtosecond Pulse Generation by Molecular Modulation, *Phys. Rev. Lett.*, Vol. 81, 2894-2897, ISSN 0031-9007

Hartemann, F. V. (1998). High-intensity scattering processes of relativistic electrons in vacuum, *Phys. Plasmas*, Vol. 5, 2037-2047, ISSN 1070-664X

Hartemann, F. V.; Brown,W. J.; Gibson, D. J.; Anderson, S. G.; Tremaine, A. M.; Springer, P. T.; Wootton, A. J.; Hartouni, E. P. & Barty, C. P. J. (2005). High-energy scaling of Compton scattering light sources, *Phys. Rev. ST AB*, Vol. 8, 100702-1-17, ISSN 1098-4402

Hentschel, M.; Kienberger, R.; Spielmann, Ch. G.; Reider, A.; Milosevic, N.; Brabec, T.; Corkum, P.; Heinzmann, U.; Drescher, M.; & Krausz, F. (2001). Attosecond metrology, *Nature*, Vol. 414, 509-513, ISSN 0028-0836

Hertz, E., Papadogiannis, N.A., Nersisyan, G., Kalpouzos, C., Halfmann, T., Charalambidis, D., and Tsakiris, G.D. (2001), Probing attosecond pulse trains using "phase-control" techniques, Phys. Rev. A, 64, (051801-1-4) 1050-2947

Huang, L.; Callan, J. P.; Glezer, E. N.; & Mazur, E. (1998). GaAs under Intense Ultrafast Excitation: Response of the Dielectric Function, *Phys. Rev. Lett.*, Vol. 80, 185-188, ISSN 0031-9007

Mourou, G. A.; Barty, C. P. J. & Perry, M. D. (1998). Ultrahigh-Intensity Lasers: Physics of the Extreme on a Tabletop, *Phys. Today*, Vol. 51, Iss. 1, 22-28, ISSN 0031-9228

Jackson, J. D. (1975). *Classical Electrodynamics*, 2nd ed., Wiley, ISBN 047143132X, New York

Kaplan, A. E. & Shkolnikov, P. L. (2002). Lasetron: A Proposed Source of Powerful Nuclear-Time-Scale Electromagnetic Bursts, *Phys. Rev. Lett.*, Vol. 88, 074801-1-4, ISSN 0031-9007

Kaplan, A.E. & Shkolnikov, P.L.(1996). Subfemtosecond pulses in the multicascade stimulated Raman scattering, *J. Opt. Soc. Am. B*, Vol. 13, 347-354, ISSN 0740-3224

Kawano, H.; Hirakawa, Y. & Imasaka, T. (1998). Generation of high-order rotational lines in hydrogen by four-wave Raman mixing in the femtosecond regime, *IEEE J. Quantum Electron.*, Vol. 34, 260-268, ISSN 0018-9197

Kien,F.L.; Liang, J.Q.; Katsuragawa, M.; Ohtsuki, K.; Hakuta, K. & Sokolov, A.V. (1999). Subfemtosecond pulse generation with molecular coherence control in stimulated Raman scattering, *Phys. Rev. A*, Vol. 60, 1562-1571, ISSN 1050-2947

Kim, D.; Lee, H.; Chung, S. & Lee, K. (2009). Attosecond keV x-ray pulses driven by Thomson scattering in a tight focus regime, *New Journal of Physics*, Vol. 11, 063050-1-12, ISSN 1367-2630

Kim, D.-E.; Toth, C. & Barty, C. P. J. (1999). Population inversion between atomic inner-shell vacancy states created by electron-impact ionization and Coster-Kronig decay, *Phys. Rev. A: Rap. Comm.*, Vol. 59, R4129-R4132, ISSN 1050-2947

Kim, D.; Son, S. H.; Kim, J. H.; Toth, C. & Barty, C. P. J. (2001). Gain characteristics of inner-shell photoionization-pumped L23M1 transition in Ca, *Phys. Rev. A*, Vol. 63, 023806-1-6, ISSN 1050-2947

Kling, M. F.; Siedschlag, Ch.; Verhoef, A. J.; Khan, J. I.; Schultze, M.; Uphues, Th.; Ni, Y.; Uiberacker, M.; Drescher, M.; Krausz, F. & Vrakking, M. J. J. (2006). Control of Electron Localization in Molecular Dissociation, *Science*, Vol. 312, 246-248, ISSN 0036-8075

Krausz, F. & Ivanov, M. (2009). Attosecond physics, *Rev. of Mod. Phys*, Vol. 81, 163-234, ISSN 0034-6861

Lee, K.; Cha, Y. H.; Shin, M. S.; Kim, B. H. & Kim, D. (2003a). Temporal and spatial characterization of harmonics structures of relativistic nonlinear Thomson scattering, *Opt. Express*, Vol. 11, 309-316, ISSN 1094-4087

Lee, K.; Cha, Y. H.; Shin, M. S.; Kim, B. H. & Kim, D. (2003b). Relativistic nonlinear Thomson scattering as attosecond x-ray source, *Phys. Rev. E*, Vol. 67, 026502-1-7, ISSN 1539-3755

Lee, K.; Kim, B. H. & Kim, D. (2005). Coherent radiation of relativistic nonlinear Thomson scattering, *Phys. Plasmas*, Vol. 12, 043107-1-8, ISSN 1070-664X

Lee, K.; Park, S. H.; Jeong, Y. U. (2006). Nonlinear Thomson Scattering for Attosecond X-ray Pulse Generation, *J. Korean Phys. Soc.*, Vol. 48, 546-553, ISSN 0374-4884

Lee, H.; Chung, S.; Lee, K. & Kim, D. (2008). A study of the Thomson scattering of radiation by a relativistic electron of a tightly-focused co-propagating femtosecond laser beam, *New Journal of physics*, Vol. 10, 093024-1-11, ISSN 1367-2630

Lichters, R.; Meyer-ter-Vehn, J. & Pukhov, A. (1996). Short-pulse laser harmonics from oscillating plasma surfaces driven at relativistic intensity, *Phys. Plasmas*, Vol. 3, 3425-3437, ISSN 1070-664X

von der Linde, D.; Engers, T.; Jenke, G.; Agostini, P.; Grillon, G.; Nibbering, E.; Mysyrowicz, A. & Antonetti, A. (1995). Generation of high-order harmonics from solid surfaces by intense femtosecond laser pulses, *Phys. Rev. A*, Vol. 52, R25-R27, ISSN 1050-2947

von der Linde, D. & Rzazewski, K. (1996). High-order optical harmonic generation from solid surfaces, *Appl. Phys. B: Lasers Opt.*, Vol. 63, 499-506, ISSN 0946-2171

von der Linde, D. (1999). Generation of high order optical harmonics from solid surfaces, *Appl. Phys. B: Lasers Opt.*, Vol. 68, 315-319, ISSN 0946-2171

Neutze, R.; Wouts, R.; van der Spoel, D.; Weckert,E. & Hajdu, J. (2000). Potential for biomolecular imaging with femtosecond X-ray pulses, *Nature*, Vol. 406, 752-757, ISSN 0028-0836

Norreys, P. A.; Zepf, M.; Moustaizis, S.; Fews, A. P.; Zhang, J.; Lee, P.; Bakarezos, M.; Danson, C. N.; Dyson, A.; Gibbon, P.; Loukakos, P.; Neely, D.; Walsh, F. N.; Wark, J. S. & Dangor, A. E. (1996). Efficient Extreme UV Harmonics Generated from Picosecond Laser Pulse Interactions with Solid Targets, *Phys. Rev. Lett.*, Vol. 76, 1832-1835, ISSN 0031-9007

Normile, D. (2006). MATERIALS SCIENCE: Japanese Latecomer Joins Race To Build a Hard X-ray Laser, *Science*, Vol. 314, 751-752, ISSN 0036-8075

Paul, P. M.; Toma, E. S.; Breger, P.; Mullot, G.; Auge, F.; Balcou, Ph.; Muller, H. G. & Agostini, P. (2001). Observation of a Train of Attosecond Pulses from High Harmonic Generation, *Science*, Vol. 292, 1689-1692, ISSN 0036-8075

Perry, M. D. & Mourou, G. (1994). Terawatt to Petawatt Subpicosecond Lasers, *Science*, Vol. 264, 917-924, ISSN 0036-8075

Perutz, M.; Wilkinson, F. A. J.; Paoli, M. & Dodson, G. G. (1998). THE STEREOCHEMICAL MECHANISM OF THE COOPERATIVE EFFECTS IN HEMOGLOBIN REVISITED, *Annu. Rev. Biophys. Biomol. Struct.*, Vol. 27, 1-34, ISSN 1056-8700

Salamin, Yousef I. & Keitel, Christoph H. (2002). Electron Acceleration by a Tightly Focused Laser Beam, *Physical Review Letters* Vol. 88, 095005, ISSN 1079-7114

Salamin, Y. I. (2007). Fields of a Gaussian beam beyond the paraxial approximation, *Applied Physics B* Vol. 86, 319-326, ISSN 1432-0649

Sarachik, E. S. & Schappert, G. T. (1970). Classical Theory of the Scattering of Intense Laser Radiation by Free Electrons, *Phys. Rev. D*, Vol. 1, 2738-2753, ISSN

Schoenlein, R. W. (2000). Generation of Femtosecond Pulses of Synchrotron Radiation, *Science*, Vol. 287, 2237-2240, ISSN 0036-8075

Sheffield, J. (1975). *Plasma Scattering of Electromagnetic Radiation*, Academic Press, ISBN 0126387508, New York

Siders, C. W.; Cavalleri, A.; Sokolowski-Tinten, K.; Toth, C.; Guo, T.; Kammler, M. H.; v. Hoegen, M. R.; Wilson, K.; v. d. Linde, D. & Barty, C. P. J. (1999). Detection of Nonthermal Melting by Ultrafast X-ray Diffraction, *Science*, Vol. 286, 1340-1342, ISSN 0036-8075

Sokolowski-Tinten, K.; Blome, C.; Blums, J.; Cavalleri, A.; Dietrich, C.; Tarasevitch, A.; Uschmann, I.; Förster, E.; Kammler, M.; Horn-von-Hoegen, M. & von der Linde, D. (2003). Femtosecond X-ray measurement of coherent lattice vibrations near the Lindemann stability limit , *Nature*, Vol. 422, 287-289, ISSN 0028-0836

Sprangle, P.; Ting, A.; Esarey, E & Fisher, A. (1992). Tunable, short pulse hard x-rays from a compact laser synchrotron source, *J. Appl. Phys.*, Vol. 72, 5032-5038, ISSN 0021-8979

Ta Phuoc, K. ; Rousse, A.; Pittman, M.; Rousseau, J. P.; Malka, V.; Fritzler, S.; Umstadter, D. & Hulin, D. (2003). X-Ray Radiation from Nonlinear Thomson Scattering of an Intense Femtosecond Laser on Relativistic Electrons in a Helium Plasma, *Phys. Rev. Lett.*, Vol. 91, 195001-1-4, ISSN 0031-9007

Ta Phuoc, K.; Fitour, R.; Tafzi, A.; Garl, T.; Artemiev, N.; Shah, R.; Albert, F.; Boschetto, D.; Rousse, A.; Kim, D-E.; Pukhov, A. & Seredov, V. (2007). Demonstration of the ultrafast nature of laser produced betatron radiation, *Phys. Plasmas*, Vol. 14, 080701.1-4, ISSN 1070-664X

Tarasevitch, A.; Orisch, A.; von der Linde, D.; Balcou, Ph.; Rey, G.; Chambaret, J. P.; Teubner, U.; Klopfel, D. & Theobald, W. (2000). Generation of high-order spatially coherent harmonics from solid targets by femtosecond laser pulses, *Phys. Rev. A*, Vol. 62, 023816-1-6, ISSN 1050-2947

Ueshima, Y.; Kishimoto, Y.; Sasaki, A. & Tajima,T. (1999). Laser Larmor X-ray radiation from low-Z matter, *Laser Part. Beams*, Vol. 17, 45-48, ISSN 0263-0346

Uiberacker, M.; Uphues,Th.; Schultze, M.; Verhoef, A. J.; Yakovlev, V.; Kling, M. F.; Rauschenberger, J.; Kabachnik, N.; Schröder, M. H.; Lezius, M.; Kompa, K. L.; Muller, H.-G.; Vrakking, M. J. J.; Kleineberg, S. U.; Heinzmann, U.; Drescher , M. & Krausz, F. (2007). Attosecond real-time observation of electron tunnelling in atoms, *Nature*, Vol. 446, 627-632, ISSN 0028-0836

Vachaspati (1962). Harmonics in the Scattering of Light by Free Electrons, *Phys. Rev*, Vol. 128, 664-666, ISSN

Vos, M. H. & Martin, J.-L. (1999). Femtosecond processes in proteins, *BBA-Bioenergetics*, Vol. 1411, 1-20, ISSN 0005-2728

Wagner, R. E.; Su, Q. & Grobe, R. (1999). High-order harmonic generation in relativistic ionization of magnetically dressed atoms, *Phys. Rev. A*, Vol. 60, 3233-3243, ISSN 1050-2947

Weller, H. R. & Ahmed, M. W. (2003). The HIγS Facility: A Free-Electron Laser Generated Gamma-Ray Beam for Research in Nuclear Physics, *Mod. Phys. Lett. A*, Vol. 18, 1569-1590, ISSN 0217-7323

Yu, W.; Yu, M. Y.; Ma, J. X. & Xu, Z. (1998). Strong frequency up-conversion by nonlinear Thomson scattering from relativistic electrons, *Phys. Plasmas*, Vol. 5, 406-409, ISSN 1070-664X

Zhou, J.; Peatross, J.; Murnane, M. M. & Kapteyn, H. C. (1996). Enhanced High-Harmonic Generation Using 25 fs Laser Pulses, *Phys. Rev. Lett.*, Vol. 76, 752-755, ISSN 0031-9007

Zewail, A. (2000). femtochemistry:atomic-scale dynamics of the chemical bond, *J. Phys. Chem. A*, Vol. 104, 5660-5694, ISSN 0021-9606

Advances in Solid State Lasers Development and Applications

Edited by Mikhail Grishin

ISBN 978-953-7619-80-0
Hard cover, 630 pages
Publisher InTech
Published online 01, February, 2010
Published in print edition February, 2010

Invention of the solid-state laser has initiated the beginning of the laser era. Performance of solid-state lasers improved amazingly during five decades. Nowadays, solid-state lasers remain one of the most rapidly developing branches of laser science and become an increasingly important tool for modern technology. This book represents a selection of chapters exhibiting various investigation directions in the field of solid-state lasers and the cutting edge of related applications. The materials are contributed by leading researchers and each chapter represents a comprehensive study reflecting advances in modern laser physics. Considered topics are intended to meet the needs of both specialists in laser system design and those who use laser techniques in fundamental science and applied research. This book is the result of efforts of experts from different countries. I would like to acknowledge the authors for their contribution to the book. I also wish to acknowledge Vedran Kordic for indispensable technical assistance in the book preparation and publishing.

How to reference

In order to correctly reference this scholarly work, feel free to copy and paste the following:

Kitae Lee, Sang-Young Chung, and Dong-Eon Kim (2010). Relativistic Nonlinear Thomson Scattering: Toward Intense Attosecond Pulse, Advances in Solid State Lasers Development and Applications, Mikhail Grishin (Ed.), ISBN: 978-953-7619-80-0, InTech, Available from: http://www.intechopen.com/books/advances-in-solid-state-lasers-development-and-applications/relativistic-nonlinear-thomson-scattering-toward-intense-attosecond-pulse

INTECH
open science | open minds

InTech Europe
University Campus STeP Ri
Slavka Krautzeka 83/A
51000 Rijeka, Croatia
Phone: +385 (51) 770 447
Fax: +385 (51) 686 166
www.intechopen.com

InTech China
Unit 405, Office Block, Hotel Equatorial Shanghai
No.65, Yan An Road (West), Shanghai, 200040, China
中国上海市延安西路65号上海国际贵都大饭店办公楼405单元
Phone: +86-21-62489820
Fax: +86-21-62489821

IntechOpen